

On the Controls of Daytime Precipitation in the Amazonian Dry Season

VIRENDRA P. GHATE

Argonne National Laboratory, Lemont, Illinois

PAVLOS KOLLIAS

*Brookhaven National Laboratory, Upton, and Stony Brook University, State University of New York,
Stony Brook, New York*

(Manuscript received 18 April 2016, in final form 30 August 2016)

ABSTRACT


The Amazon plays an important role in the global energy and hydrological budgets. The precipitation during the dry season (June–September) plays a critical role in maintaining the extent of the rain forest. The deployment of the first Atmospheric Radiation Measurement (ARM) Mobile Facility (AMF-1) in the context of the Green Ocean Amazon (GOAmazon) field campaign at Manacapuru, Brazil, provided comprehensive measurements of surface, cloud, precipitation, radiation, and thermodynamic properties for two complete dry seasons (2014 and 2015). The precipitation events occurring during the nighttime were associated with propagating storm systems (nonlocal effects), while the daytime precipitation events were primarily a result of local land–atmosphere interactions. During the two dry seasons, precipitation was recorded at the surface on 106 days (43%) from 158 rain events with 82 daytime precipitation events occurring on 64 days (60.37%). Detailed comparisons between the diurnal cycles of surface and profile properties between days with and without daytime precipitation suggested the increased moisture at low and midlevels to be responsible for lowering the lifting condensation level, reducing convective inhibition and entrainment, and thus triggering the transition from shallow to deep convection. Although the monthly accumulated rainfall decreased during the progression of the dry season, the contribution of daytime precipitation to it increased, suggesting the decrease to be mainly due to reduction in propagating squall lines. The control of daytime precipitation during the dry season on large-scale moisture advection above the boundary layer and the total rainfall on propagating squall lines suggests that coarse-resolution models should be able to accurately simulate the dry season precipitation over the Amazon basin.

1. Introduction

The Amazon forest stores a substantial amount of carbon in its biomass (Saatchi et al. 2011; Gloor et al. 2012). Precipitation plays a regulating role of the Amazon rain forest canopy at various time scales (e.g., Aragao et al. 2008; Phillips et al. 2009; Toomey et al.

2011; Saatchi et al. 2013). The region is a part of the South American monsoon system (SAMS) that is characterized by two distinct seasons, a wet season from October to May and a dry season from June to September, with regional differences in the duration and onset of the two seasons (Liebmann and Mechoso 2011; Raia and Cavalcanti 2008). Rainfall occurs during both wet and dry seasons, with the rainfall in the dry season being crucial for maintaining the rain forest (Toomey et al. 2011; Lewis et al. 2011). Most of the global climate model (GCM) simulations that are part of the Intergovernmental Panel on Climate Change (IPCC) Fifth Assessment Report (AR5) forecast the Amazon forest to go through severe changes in meteorology and climate in the future, with a reduction in its extent primarily due to a drier and longer dry season (Cook et al. 2012; Joetzer et al. 2013). The rainfall in the dry season is affected by many factors, including the sea surface temperatures (SSTs) in the tropical Atlantic and Pacific

 Denotes Open Access content.

 Supplemental information related to this paper is available at the Journals Online website: <http://dx.doi.org/10.1175/JHM-D-16-0101.s1>.

Corresponding author address: Virendra P. Ghatе, Environmental Sciences, Argonne National Laboratory, 9700 S. Cass Ave., Lemont, IL 60439.
E-mail: vgate@anl.gov

DOI: 10.1175/JHM-D-16-0101.1

Oceans (Grimm 2003, 2004; Misra 2008; Fernandes et al. 2015; Yoon 2016), moisture recycling due to evaporation (Juarez et al. 2007; Spracklen et al. 2012), and local effects (Li and Fu 2004; Tanaka et al. 2014; dos Santos et al. 2014; Fitzjarrald et al. 2008).

A number of observational (Harriss et al. 1988; Kaufman et al. 1998; Silva Dias et al. 2002a) and modeling (Werth and Avissar 2002; Anber et al. 2015; Harper et al. 2014; de Gonçalves et al. 2013) studies have been conducted with the goal of improving our understanding of the controls of precipitation and the hydrological cycle in Amazonia. Despite these efforts, considerable disagreement exists in the present-climate GCM simulation of the precipitation in the Amazon region. This is partly due to our limited understanding of the processes responsible for causing precipitation during the dry season (Malhi et al. 2009; Mehran et al. 2014). Precipitation occurs at all hours during the dry season, with the number of precipitation events decreasing during the progression of the dry season (Fig. 1; Tanaka et al. 2014). The nighttime precipitation is due to the passage of storm systems that originate at a different region and hence is due to nonlocal effects (Rickenbach 2004). However, the daytime precipitation occurs because of local land–atmosphere interactions (Fitzjarrald et al. 2008). Here, observations collected during the Green Ocean Amazon (GOAmazon) field campaign are used to study the controls of daytime (local) precipitation during the Amazon dry season. In particular, the presented study aims to address the following questions: 1) Which factors control the daytime transition from shallow (nonprecipitating) to deep (precipitating) convection? and 2) What causes the number of precipitation events to decrease as the dry season progresses? Hence, although the study reports the characteristics (amount, duration, etc.) of precipitation events, the focus is on the factors responsible for forming precipitation-producing clouds.

To answer the above questions, we have used the data collected by the first Atmospheric Radiation Measurement (ARM) Mobile Facility (AMF-1) during the GOAmazon field campaign (<http://www.arm.gov/sites/amf/mao/>). Data collected during the 2014 and 2015 dry seasons (June–September) are used in this study and are described in section 2. The mean diurnal cycle of surface meteorology, thermodynamics, and clouds during the dry season is described in section 3. Subsequently, the differences in the diurnal cycle of days with daytime precipitation and days with cumulus clouds (nonprecipitating) are described in section 4. The progression of the daily averaged values of a few key parameters during the dry season is studied in section 5 in the context of daytime precipitation events.

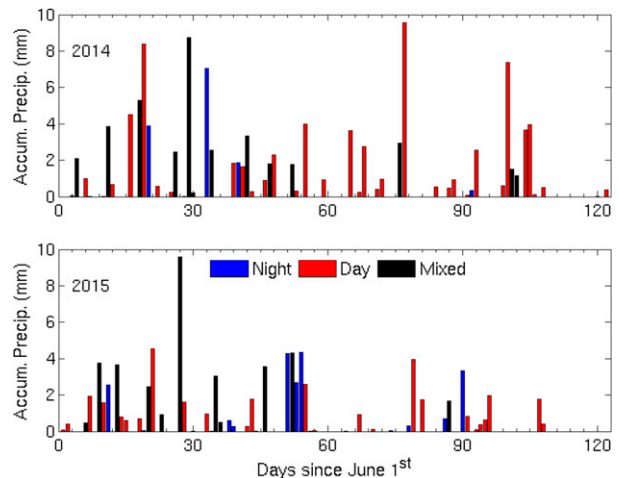


FIG. 1. Daily accumulated precipitation during the dry season of (top) 2014 and (bottom) 2015. Precipitation was observed on 106 days (43%) from the total 244 days, 54 days in 2014 and 52 days in 2015. The rain events were classified as daytime if they occurred between 0900 and 2100 LT, nighttime if they occurred between 2100 and 0900 LT, and mixed if they occurred during both. Thus, 64 rain events were identified as daytime, 16 as nighttime, and 26 as mixed.

The article is concluded with a summary, conclusions, and discussion section.

2. Data and instrumentation

The AMF-1 was deployed at Manacapuru, Brazil (3.2°S, 60.5°W; 50 m), for the GOAmazon field campaign from January 2014 to December 2015. In this study, the dry season is defined from 1 June to 30 September, similar to Harper et al. (2014). The AMF-1 instrumentation includes a vertically pointing Doppler cloud radar, lidars, and radiometers. Below, we have only described the instruments' data that were used in this study. A detailed description of the AMF-1 instrumentation can be found in Mather and Voyles (2013).

A vertically pointing 94-GHz Doppler cloud radar known as the W-band ARM Cloud Radar (WACR) was part of the AMF-1. The WACR reports the full Doppler spectrum and its first three moments at 2-s temporal and 30-m range resolutions. Also, part of the AMF-1 was a laser ceilometer that operated at 905-nm wavelength and reported the values of the first three cloud-base heights at 15-s temporal and 30-m range resolution. The WACR and ceilometer data were combined to produce estimates of noise-filtered radar reflectivity, cloud boundaries, and cloud fraction as described by Kollias et al. (2009) at 5-s temporal and 30-m range resolutions. A microwave radiometer (MWR) reported the sky brightness temperatures at 23.8 and 31.4 GHz, from which the column integrated water vapor (IWV) and liquid water path (LWP) were

retrieved at a 20-s resolution. Also, part of the AMF-1 instrumentation was a surface meteorological station that reported temperature, moisture, pressure, and winds every minute. The minute values of rain rate as reported by the present weather detector (PWD) system that operates at 875 nm and has a sensitivity of 0.05 mm h^{-1} were used in this study. The height of the lifting condensation level (LCL) was calculated using the formulation provided by Bolton (1980) from the meteorological station data. Half-hourly values of surface sensible heat flux (SHF), latent heat flux (LHF), and surface friction velocity U^* were calculated using the data collected by the eddy correlation (ECOR) flux measurement system. A Surface Energy Balance System (SEBS) reported the ground heat flux and the net ecosystem exchange (SHF + LHF) on half-hourly time scales. Because of persistent failure in a component of the ECOR LHF sensor, the ECOR-reported LHF measurements were intermittent. Additionally, at times with lower wind speeds at night ($<1 \text{ m s}^{-1}$), the 30-min period used to calculate the eddy covariances was not sufficient to capture the large eddies within the boundary layer. Hence, a second estimate of LHF is calculated from SEBS measurements by subtracting the ECOR-reported SHF from the SEBS-reported net ecosystem exchange. Hereafter, this flux is referred as the SEBS LHF. The differences in the values of SEBS LHF and ECOR LHF are caused by energy imbalance (Wohlfahrt and Widmoser 2013; Burba 2013), with SEBS LHF being mostly higher than ECOR LHF. It is beyond the scope of this article to probe the causes of this difference; however, we believe the SEBS LHF to be much closer to the real exchange of moisture between the surface and the atmosphere than the ECOR LHF (D. Cook 2016, personal communication).

Minute values of upwelling and downwelling radiation in the shortwave and longwave spectrum were measured by the radiation platform. Balloon-borne radiosondes were launched every 6 h (0600, 1200, 1800, and 0000 UTC) that measured the tropospheric temperature, moisture, pressure, and wind fields. The local time (LT) was 4 h behind the UTC. The convective inhibition (CIN) and convective available potential energy (CAPE) were calculated from the profiles of equivalent potential temperature θ_e and saturation equivalent potential temperature θ_{es} using the method described by Kollias et al. (2009). The 50-m value of θ_e was used as a proxy for the surface value to avoid surface layer effects, and the level with θ_{es} value equal to that was termed as the level of free convection (LFC). Similar to Gentine et al. (2013), we calculated the lapse rate of potential temperature θ and water vapor mixing ratio q between 1 and 3 km and referred to them as $(\partial\theta/\partial z)$ and $(\partial q/\partial z)$ where z refers to height. The convective triggering potential (CTP), the low-level humidity index

HI_{low} , and the inversion Bowen ratio B_{inv} were calculated using the definition by Findell and Eltahir (2003), with CTP and B_{inv} calculated for the 1–3-km layer and HI_{low} calculated for the 500–1500-m layer.

The horizontal winds were retrieved every 15-min from the plan position indicator (PPI) scans performed by the Doppler lidar (DL) that operated at 1.5- μm wavelength and 30-m range resolution. The hourly output from the European Centre for Medium-Range Weather Forecasts (ECMWF) Re-Analysis operating at 137 levels and 0.56° grid resolution is used to characterize the large-scale environment. In particular, ECMWF reported large-scale vertical velocity, and the horizontal advection tendency of temperature and moisture are used in this study. The model output reported the total and physical tendency of temperature and moisture every hour, from which the horizontal advection terms of temperature and moisture were calculated. The hourly averaged values of the aforementioned parameters are used to calculate the diurnal cycle (sections 3 and 4) and the daily mean values (section 5).

3. Average diurnal cycle

The average diurnal cycle was calculated using hourly values of respective parameters, with the hourly averages calculated for hours at the beginning of the hour; for example, the zeroth hour corresponds to values between 0000 and 0100 LT and the eleventh hour corresponds to values between 1100 and 1200 LT.

The average diurnal cycle of the surface meteorological parameters during the dry season is shown in Fig. 2. The average surface air temperature was a minimum at 0600 LT, followed by a rapid increase until about 1100 LT, and then remained constant until 1600 LT. The range of the temperature as denoted by the standard deviation bars suggests greater fluctuations in daytime temperatures than in the nighttime temperatures. The averaged water vapor mixing ratio at the surface was also a minimum at 0600 LT, but was highest at 0800 LT followed by another local minimum at 1500 LT and maximum at 1900 LT. It is difficult to explain the cause of the two peaks (and minimum) in the diurnal cycle of the mixing ratio from these observations. The latter might be due to the loss of mixed layer water vapor to the free troposphere and deepening of the mixed layer, thereby redistributing the vapor over a deeper layer, with the total loss not being compensated by the LHF. The winds at the surface were northerly and weak ($<1 \text{ m s}^{-1}$) during nighttime and easterly during the daytime, with a peak speed of 3 m s^{-1} at noon. Similar to de Oliveira and Fitzjarrald (1993, 1994), the deviations of hourly averaged surface winds from the diurnal mean

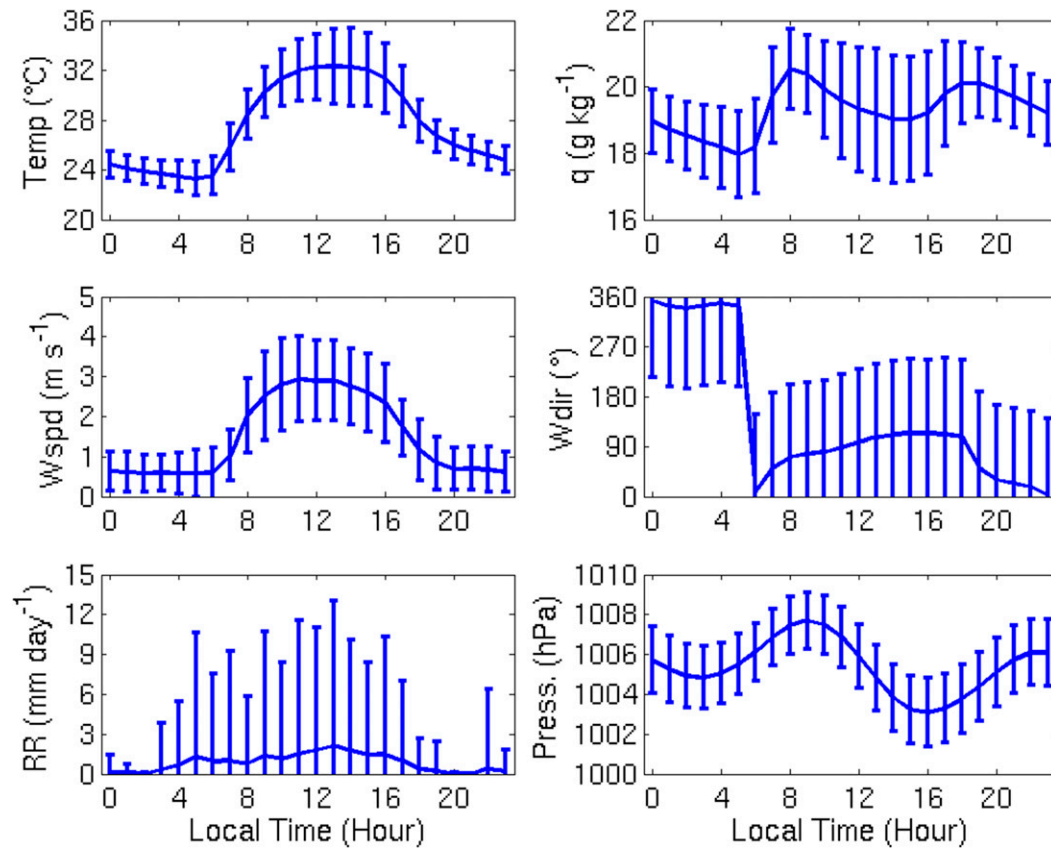


FIG. 2. Mean diurnal cycle of the (top left) surface air temperature, (top right) mixing ratio, (middle left) wind speed, (middle right) wind direction, (bottom left) rain rate, and (bottom right) surface pressure during the dry season. The bars denote one std dev.

were termed as the thermal circulations. The polar plot of the averaged thermal circulation (not shown) exhibited an elliptical trajectory that rotated clockwise with time consistent with previous observations. The rain rate did not exhibit a distinct diurnal cycle, as in other parameters with the standard deviation values much greater than the means, suggesting a large variability in the amount and timing of rain events. The surface pressure at AMF-1 also exhibited a distinct diurnal cycle with minimums at 0300 and 1600 LT and maximums at 0900 and 2300 LT. Broadly synthesizing the mean diurnal cycle of meteorological parameters at Manacapuru during the dry season follows the classic summertime diurnal cycle of continental boundary layer shown by Stull (1988) and the diurnal cycles reported in that region (e.g., Tanaka et al. 2014). The diurnal changes in the winds and pressure are consistent with the previous findings of a river breeze resulting because of temperature and pressure contrast between the land surface and the river (de Oliveira and Fitzjarrald 1993).

The mean diurnal cycle of SHF, LHF, and U^* during the dry season is shown in Fig. 3. The SHF and LHF

were near zero at night and exhibited maximum values around noon (ECOR SHF $\sim 100 \text{ W m}^{-2}$, ECOR LHF $\sim 250 \text{ W m}^{-2}$, and SEBS LHF $\sim 400 \text{ W m}^{-2}$). The higher value of LHF than SHF is consistent with water-saturated land conditions despite the dry season. The standard error of the mean of ECOR SHF is higher than both the ECOR LHF and SEBS LHF, implying relative changes in SHF to be greater than those in the LHF. The surface friction velocity is very low ($< 0.1 \text{ m s}^{-1}$) at nighttime, with a peak of $\sim 0.25 \text{ m s}^{-1}$ at noon. The surface convective velocity scale w^* exhibited a diurnal cycle similar to the SHF and LHF with a peak of $\sim 1.4 \text{ m s}^{-1}$ at noon (not shown). The significantly lower value of U^* compared to w^* suggests the role of shear in maintaining turbulence within the boundary layer to be smaller than that of the surface turbulent fluxes.

The mean diurnal cycle of downwelling shortwave radiation (SWD), upwelling shortwave radiation (SWU), downwelling longwave radiation (LWD), and upwelling longwave radiation (LWU) at the surface is shown in Fig. 4. The downwelling and upwelling shortwave radiation follows the solar cycle with a Gaussian

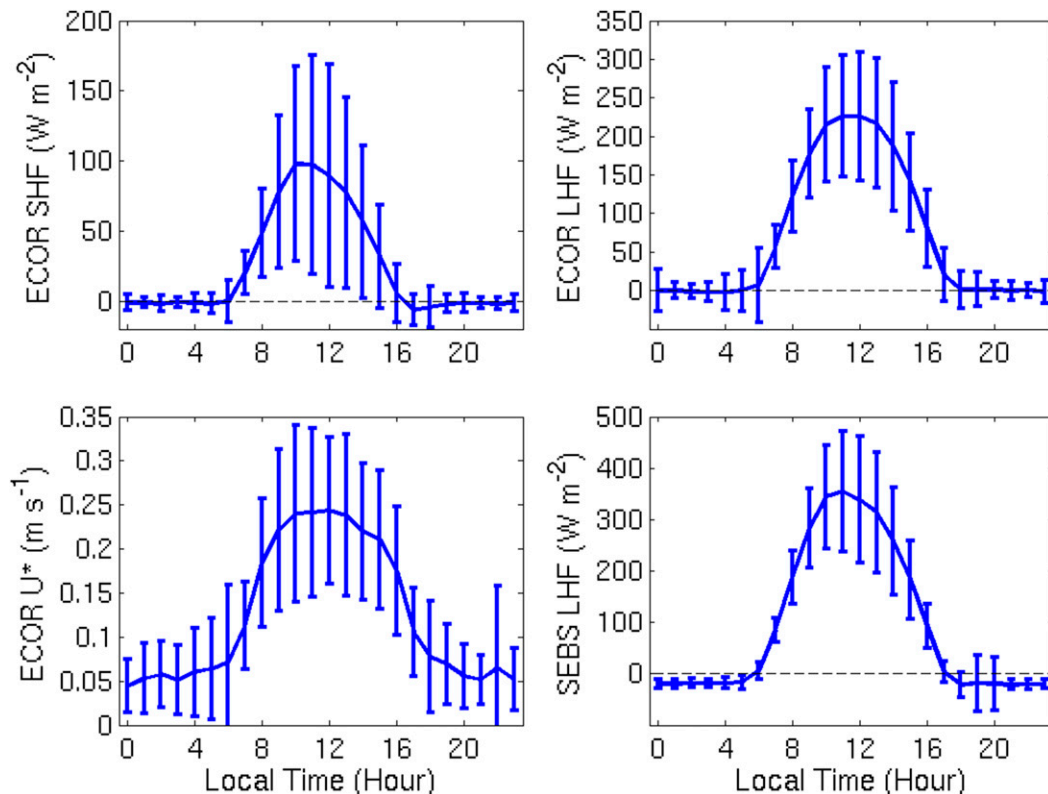


FIG. 3. Mean diurnal cycle of surface (top left) ECOR SHF, (top right) ECOR LHF, (bottom left) ECOR friction velocity, and (bottom right) SEBS LHF during the dry season.

shape and peak around noon. The average shortwave albedo of the land is about 0.20 with standard deviation of 0.02. Broken cloud conditions are responsible for the observed SWD standard deviation; however, no significant departure from the Gaussian shape is observed. The diurnal cycle of LWD loosely follows that of surface air temperature with an almost constant value at night of $\sim 400 \text{ W m}^{-2}$, with a rapid increase to a peak value of $\sim 425 \text{ W m}^{-2}$ near noon, followed by a gradual decrease. This is expected as the cloud coverage is low ($< 25\%$), and for the same amount of water vapor, an 8-K increase in the temperature will roughly cause an increase in the longwave flux by $\sim 44 \text{ W m}^{-2}$ (11%). The diurnal cycle of LWU follows the solar cycle with values of $\sim 440 \text{ W m}^{-2}$ at night and a peak of $\sim 525 \text{ W m}^{-2}$ around noon, followed by a gradual decrease. The net longwave flux at the surface is always negative, denoting transfer of heat from the surface to the atmosphere. This is consistent with the low negative values of SHF and LHF during nighttime. The LWP and IWV as reported by the MWR did not exhibit a distinct average diurnal cycle (Fig. 4). Although the averaged LWP exhibited a local peak near noon, the standard error of the mean was much higher during that time. The IWV was $\sim 4.6 \text{ cm}$ during the entire day with a standard deviation of $\sim 0.6 \text{ cm}$.

Radiosondes were launched four times a day at 0200, 0800, 1400, and 2000 LT (Fig. 5). Noticeably, apart from the near-surface values, the averaged profiles did not exhibit significant changes with height. On average, the potential temperature increased with height and the mixing ratio decreased with height in all soundings, suggesting the atmosphere to be statically stable, except for a weak mixed layer in the 1300 LT averaged sounding. The averaged wind speed increased almost linearly with height from the surface to 2 km in all of the soundings and then remained almost constant. The wind direction was northeasterly in the lower 2 km in the 0200 and 0800 LT soundings and was easterly in the 1400 and 2000 LT soundings. Above 2 km the winds were easterly at all times. Although similar to the J1-type profile shown by [de Oliveira and Fitzjarrald \(1993\)](#), a vertical directional wind shear was observed below 1 km, unlike their observations, and the maximum of the wind speed was at a higher altitude ($\sim 2 \text{ km}$) and did not change with time. The profiles of wind speed and wind direction as reported by the DL also did not show any presence of nocturnal low-level jet. The mean profiles of equivalent potential temperature and saturation equivalent potential temperature suggested CAPE and CIN to be present during all sounding launch times, with lowest CIN

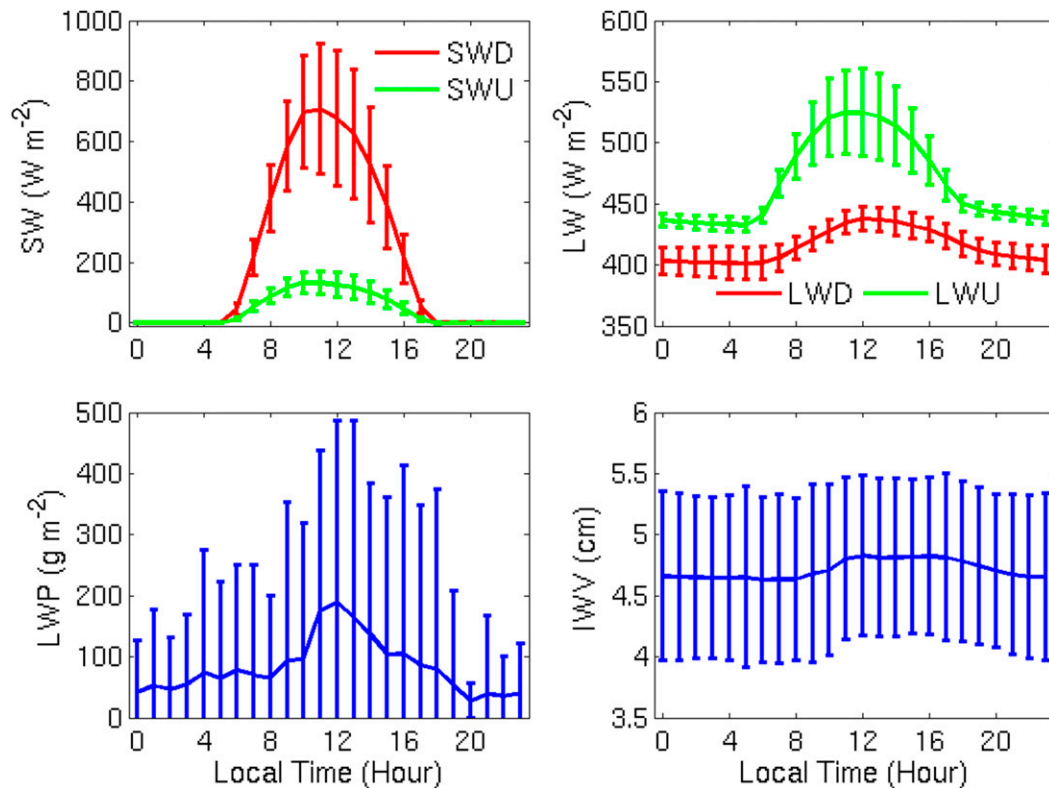


FIG. 4. Diurnal cycle of (top left) SWU and SWD at the surface, (top right) LWU and LWD at the surface, (bottom left) LWP, and (bottom right) IWV.

values at 0800 LT and highest CAPE values at 1400 LT. The average CAPE and CIN at 0800 LT were 758.31 and -88.66 J kg^{-1} , while the same at 1400 LT were 681.40 and $-136.91 \text{ J kg}^{-1}$, respectively. The average diurnal cycle of wind speed and wind direction as reported by the DL (not shown) was consistent with that from the surface meteorological station and the soundings.

The average diurnal cycle of hydrometeor fraction, LCL, and first cloud-base height during the dry season is shown in Fig. 6. The LCL was near surface during the nighttime and peaked to a value of 1065 m at 1500 LT. The higher values of hydrometeor fraction ($>20\%$) are seen for the low-level clouds during the daytime and high-level clouds during the later afternoon and at night. As the radar pulse of the WACR is susceptible to attenuation due to water vapor and liquid water, the deduced coverage of high-level clouds might be underestimated. Cirrus clouds are regularly observed over the Amazon with coverage of $\sim 55\%$ during the dry season (Gouveia et al. 2016, manuscript submitted to *Atmos. Chem. Phys. Discuss.*). As data from micropulse lidar (MPL) was not used in this study, and the presence of high-level clouds was only detected from the WACR, the reported coverage of high-level clouds represents a lower bound. However, the maximum hourly averaged

rain rate observed at the surface during the study period was 4.94 mm h^{-1} , with only 0.5% of the minute values higher than 5 mm h^{-1} , suggesting the attenuation due to rainwater to be minimal. The close matching of LCL and first cloud-base height to the higher coverage of low-level clouds between 0900 and 1700 LT confirm the clouds to result from surface-based convection rather than advection. The differences in the LCL and the cloud-base height during the nighttime together with near-zero SHF and LHF suggest the boundary layer to be decoupled from the surface during these times, consistent with previous studies (Martin et al. 1988; Fitzjarrald and Moore 1990). The coverage of low-level clouds is $\sim 8\%$ from 0300 to 0800 LT and is discussed later in section 4. The high-level clouds are possibly a result of deep convection around the ARM site, consistent with a peak in late afternoon and $\sim 10\%$ coverage around midnight. As the tropical cirrus clouds typically last for 19–30 h, advecting over 600–1000 km (Luo and Rossow 2004), it is plausible for the origin of these clouds to be at a location with conditions far different than those at the AMF-1.

The average diurnal cycle of large-scale vertical velocity and of the large-scale horizontal advective tendencies of temperature and moisture are shown in Fig. 7. On average, nighttime horizontal advection is weak.

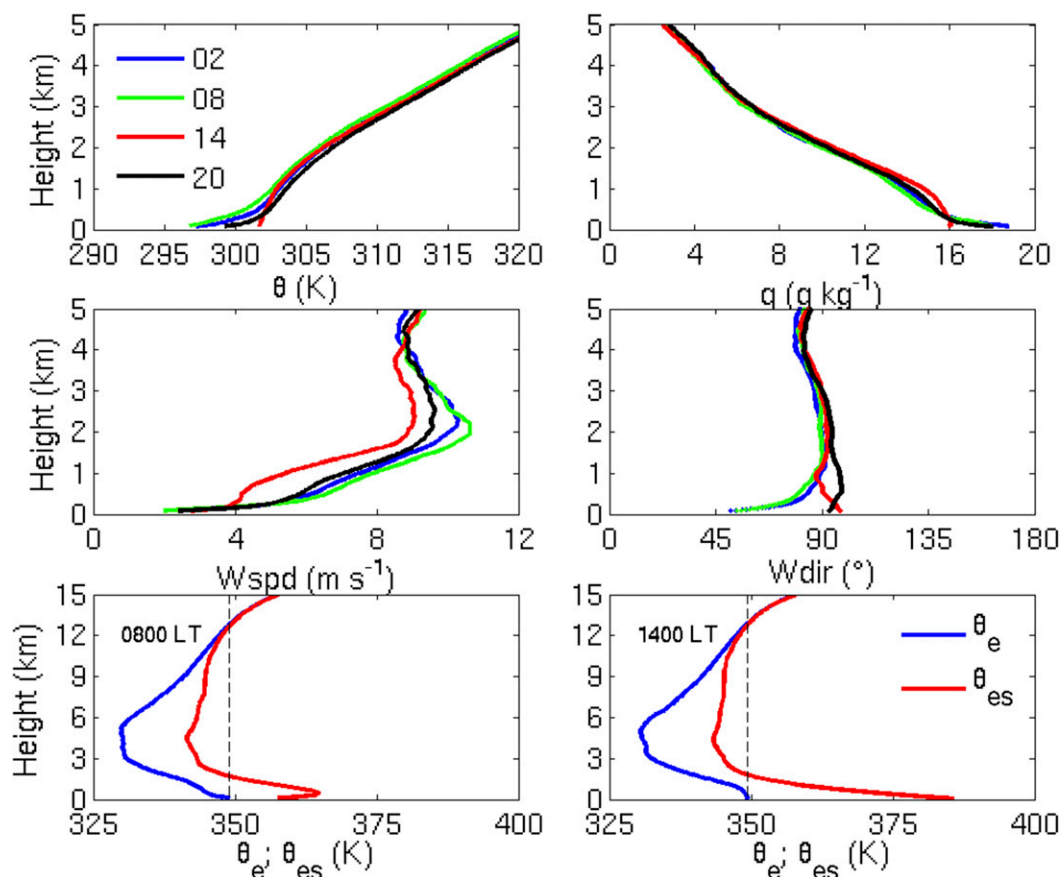


FIG. 5. Mean profile of (top left) potential temperature, (top right) water vapor mixing ratio, (middle left) wind speed, and (middle right) wind direction as reported by the soundings launched four times a day during the dry season. (bottom) The average profiles of equivalent potential temperature and saturation equivalent potential temperature from the 0800 and 1400 LT soundings.

During daytime (0800–1600 LT) a shallow cold air advection confined below 900 hPa is observed. The depth of the cold air advection during the daytime is on average consistent with the depth of the easterly wind layer shown in the soundings (Fig. 5) and the changes in the surface pressure caused by the thermal gradient between the land and river. The depth of this layer is consistent with that reported by the previous studies (de Oliveira and Fitzjarrald 1993). Above this shallow layer, the advection is warm throughout the day. On average around local noon, a moist advection is present from 950 to 750 hPa. Consistent with the tropical location, the large-scale vertical velocity follows the solar cycle and is weak during the nighttime, with high negative values (upward motion) from 0800 to 1600 LT and a peak around noon at 950 hPa. It is difficult to explain the positive moisture advection around noon that coincides with the large-scale upward motion. The low-level cloudiness simulated by the ECMWF model (not shown) peaks between 0800 and 1200 LT and hence is

inconsistent with the peak in the noontime peak in the large-scale vertical velocity.

4. Diurnal cycle during cumulus and precipitation days

Cloudy days are classified with respect to their potential to produce measurable precipitation at the ground in two categories: “cumulus” if no precipitation is measured and “precipitating” if precipitation is measured with rain rates higher than 0.05 mm h^{-1} . The classification follows that proposed by Zhang and Klein (2010, 2013). A total of 244 days were analyzed (122 over 2 years). Low-level clouds were omnipresent throughout the two dry seasons, and only 4 days (2%) are classified as “clear sky” with maximum ceilometer cloud fraction lower than 5%. Although the ceilometer-recorded cloud fraction was less than 5% on these days, the Total Sky Imager (TSI) reported the presence of shallow clouds at the ARM site. Precipitation was recorded at the surface

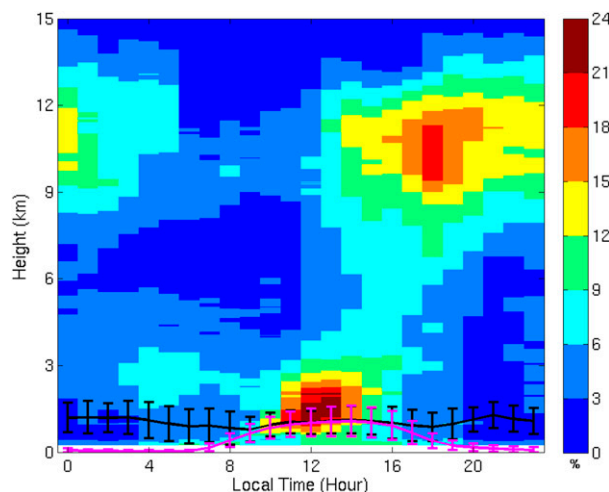


FIG. 6. Averaged diurnal cycle of hydrometeor fraction as reported by the ARM Active Remote Sensing of Clouds (ARSCL) product. The black line shows the mean cloud-base height from the ceilometer while the magenta line indicates the LCL calculated from the surface measurements.

on 106 days (43.44%). Precipitation days were further classified as daytime (0900–2100 LT), nighttime (2200–0900 LT), or mixed (daytime and nighttime) based on the time of occurrence of the precipitation events as captured by the surface rain gauge. Based on this classification, 64 days were classified as daytime precipitation, 16 days were classified as nighttime precipitation, and 26 days were classified as mixed. As reported by previous studies (e.g., Tanaka et al. 2014; Pereira Filho et al. 2002), the nighttime precipitation occurring over that region is mostly due to propagating storm systems and not produced by local effects. Additionally, the wind direction was southerly during the nighttime events (not shown), while it was similar to the average (Fig. 2) during daytime events. Here, we have focused on the causes of daytime precipitation that might have local controlling factors. Therefore, the term daytime is omitted and we focus only the mean diurnal cycle of cumulus-only days (139 days) and precipitation days (64 days). To gain insights on the continuity of convection, we also contrasted the diurnal cycles of cumulus and precipitation days that were preceded by cumulus days. Cumulus days that were preceded by cumulus days were termed as CuToCu and the daytime precipitation days that were preceded by cumulus days were termed as CuTo-Precip. A total of 89 CuToCu days and 30 CuToPrecip days were identified. The conclusions from this comparison between the averaged diurnal cycle of CuToCu and CuToPrecip days were similar to those discussed below, and the comparison plots and a table are provided as supplemental material. As the start times of most of the daytime rain events was around noon, we have only discussed variables that exhibited differences before noon for

the classification, as it is not possible to distinguish if the afternoon observations are consequences of the rain or are characteristics of the environment responsible for producing the rain.

The averaged diurnal cycle of hydrometeor fraction for cumulus days and precipitation days along with that of LCL and first cloud-base height is shown in Fig. 8. The LCL was lower during precipitation days than that during cumulus days. Most of the precipitation occurred between 1100 and 1700 LT and convective anvil outflow is observed over the site for the rest of the day. Most of the rainfall occurred between 1200 and 1600 LT during the daytime precipitation days. High-level cirrus clouds were also observed in the later afternoon and the nighttime during cumulus days as well but with lower coverage and thicknesses. We suspect the cirrus clouds to be present from 0600 to 1200 LT during precipitation days, as reliable lidar data are not available during high sun-angle conditions, and the sensitivity of the radar decreases at higher-range gates because of the range correction term. The nighttime occurrence of low-level clouds was higher during precipitation days than during cumulus days. This is broadly consistent with the hypothesis of Anber et al. (2015) regarding the presence of low-level fog during precipitating days.

Surface meteorological parameters for cumulus and precipitation days are shown in Fig. 9. The surface air temperature from 0800 to 2400 LT was lower during precipitation days than that during cumulus days. The water vapor mixing ratio at the surface was higher during precipitation days than that during cumulus days from 0900 to 1800 LT. The differences in temperature and mixing ratio are significant even before the occurrence of the precipitation events, suggesting different surface layer thermodynamics on precipitation days than cumulus days. The wind speeds were lower during precipitation days from 0800 to 1700 LT than during cumulus days. The winds were northerly during the nighttime and easterly during the daytime during each distinction. The polar plot of the thermal wind (not shown) exhibited a clockwise rotation for both distinctions, with slightly lower values of the thermal wind during precipitation days. This is consistent with similar diurnal cycle of surface pressure for the distinction with slightly higher values during precipitation days. The similar diurnal cycles of winds and pressure for the distinction suggest the effect of river breeze to be similar for the distinction.

The average diurnal cycles of surface turbulent fluxes, friction velocity, and LCL during cumulus and precipitation days are shown in Fig. 10. The SHF and LHF were lower during precipitation days than that during cumulus days from 0800 to 1700 LT. The differences in the LHF and SHF occurred before the occurrence of

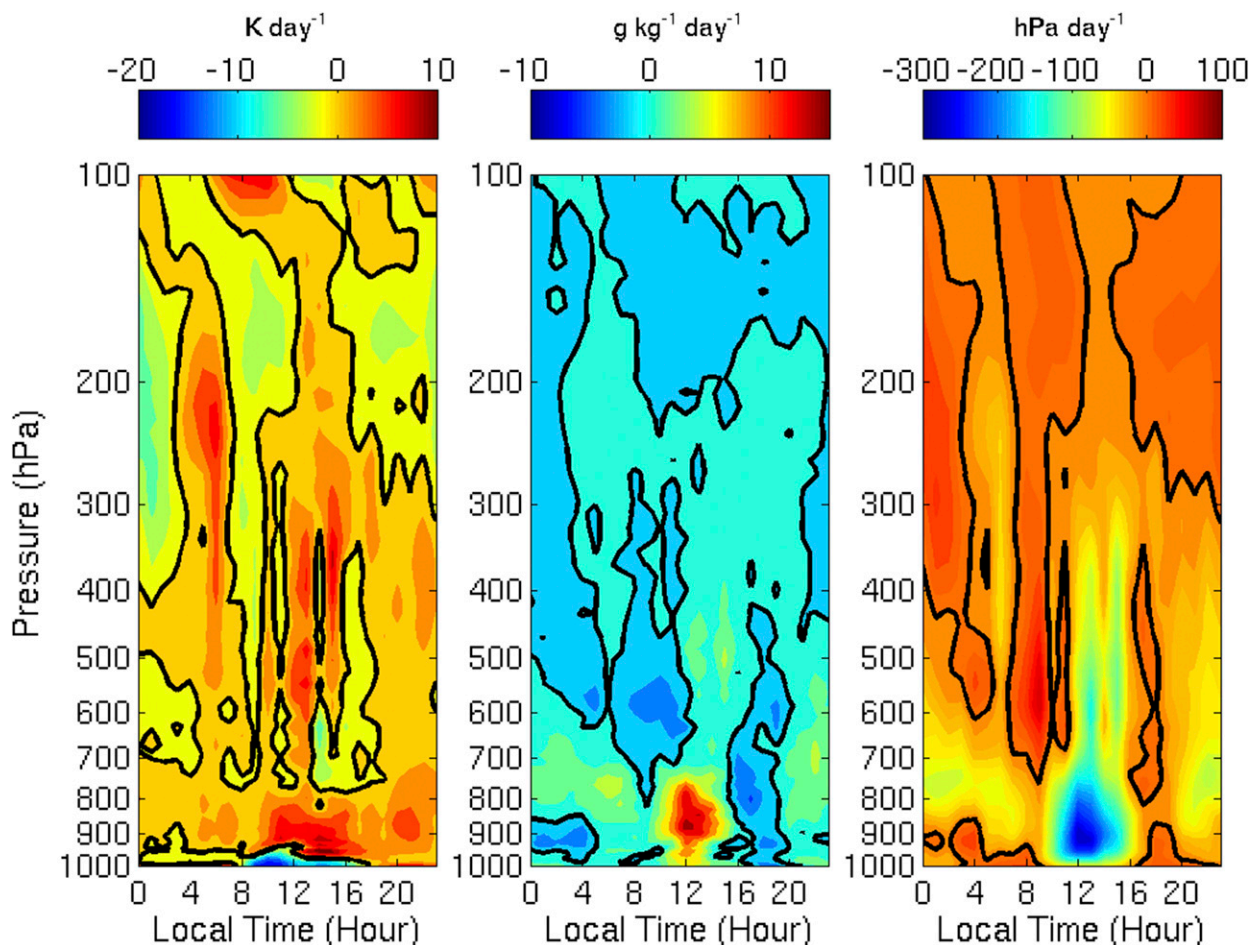


FIG. 7. Averaged diurnal cycle of horizontal advection of (left) temperature, (center) horizontal advection of moisture, and (right) large-scale vertical velocity in the lower troposphere during the dry season as reported by the ECMWF Re-Analysis. The black lines denote the zero-value contour in each panel.

precipitation; thus, it is difficult to speculate if it is caused by the precipitation and associated cloudiness. The surface friction velocity was lower during precipitation, although a 0.05 m s^{-1} (10%) reduction in the value of U^* seems insignificant to cause substantial changes in the boundary layer turbulence. The average LCL peaked at a value of $\sim 800 \text{ m}$ at 1100 LT on precipitation days, while it peaked later at 1500 LT at a value of $\sim 1300 \text{ m}$ during cumulus days. This is consistent with the presence of lower near-surface air temperature and higher mixing ratio during precipitation days.

The mean diurnal cycle of radiative fluxes, LWP, and IWV for precipitation and cumulus days is shown in Fig. 11. The SWD is substantially lower during precipitation days because of the higher cloud cover (Fig. 8). The higher cloud cover during precipitation days is also consistent with the higher values of LWD from midnight until local noon. Consistent with lower surface temperature, the LWU was lower during precipitation days. As

expected, because of the higher cloud cover and cloud thickness, the LWP was higher during precipitation days than that during cumulus days. The values of IWV were substantially higher during all hours during precipitation days. The higher statistical significance of these differences along with higher values of relative changes make the IWV the most robust parameter to differ for the distinction among the analyzed variables.

The profile of potential temperature at 0800 LT did not exhibit any significant differences between cumulus and precipitation days (Fig. 12). A mixed layer extending from the surface to 1 km is clearly visible in the averaged 1400 LT sounding for cumulus days, while for precipitation days the profile of potential temperature was statically stable in the entire lower troposphere. The statically stable profile of potential temperature might be due to the evaporatively driven downdrafts part of the precipitation events (Betts et al. 2002). The mixing ratio was higher during precipitation days at all heights

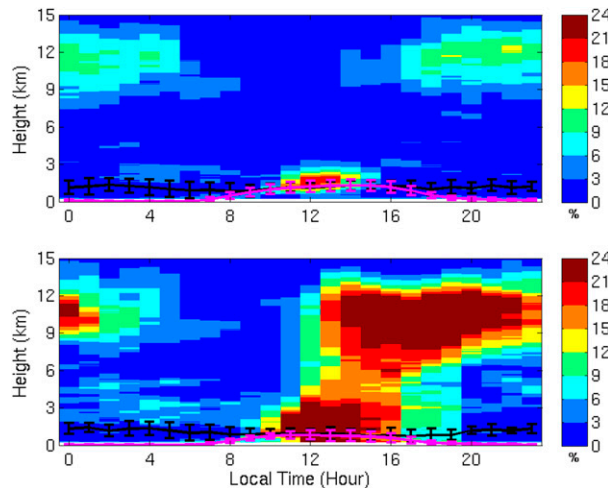


FIG. 8. Diurnal cycle of hydrometeor fraction, first cloud-base height (black), and LCL (magenta) for (top) cumulus and (bottom) daytime precipitation days. The vertical bars in LCL and cloud-base height denote one std dev.

in the 0800 and 1400 LT soundings, except for near-similar values from 1 to 2 km in the 1400 LT sounding. The lower values of mixing ratio and slightly higher values of temperature during cumulus days resulted in

lower values of equivalent potential temperature and higher values of saturation equivalent potential temperature during cumulus days than during precipitation days. This essentially resulted in lower values of CIN during precipitation days than during cumulus days. The average CIN at 0800 LT was -98.94 J kg^{-1} during cumulus days and -76.40 J kg^{-1} during precipitation days, while the average CAPE was 824.93 J kg^{-1} during cumulus days and 846.52 J kg^{-1} during precipitation days. In summary, the lower surface air temperature and higher mixing ratio at all levels during precipitation days than those during cumulus days collectively result in significantly lower CIN and slightly higher CAPE during precipitation days than those during cumulus days.

The daytime cold air advection below 900 hPa is slightly weaker and shallower during precipitation days than during cumulus days (Fig. 13), consistent with lower temperature over land (AMF-1) reducing the effect of the river breeze. The warm advection around 200 hPa is due to 16 of the daytime precipitation events being preceded by nighttime events or mixed events. This upper-level heating is absent in the CuToCu and CuToPrecip comparisons available in the supplemental material. Below the 700-hPa level ($\sim 3 \text{ km}$), the moisture

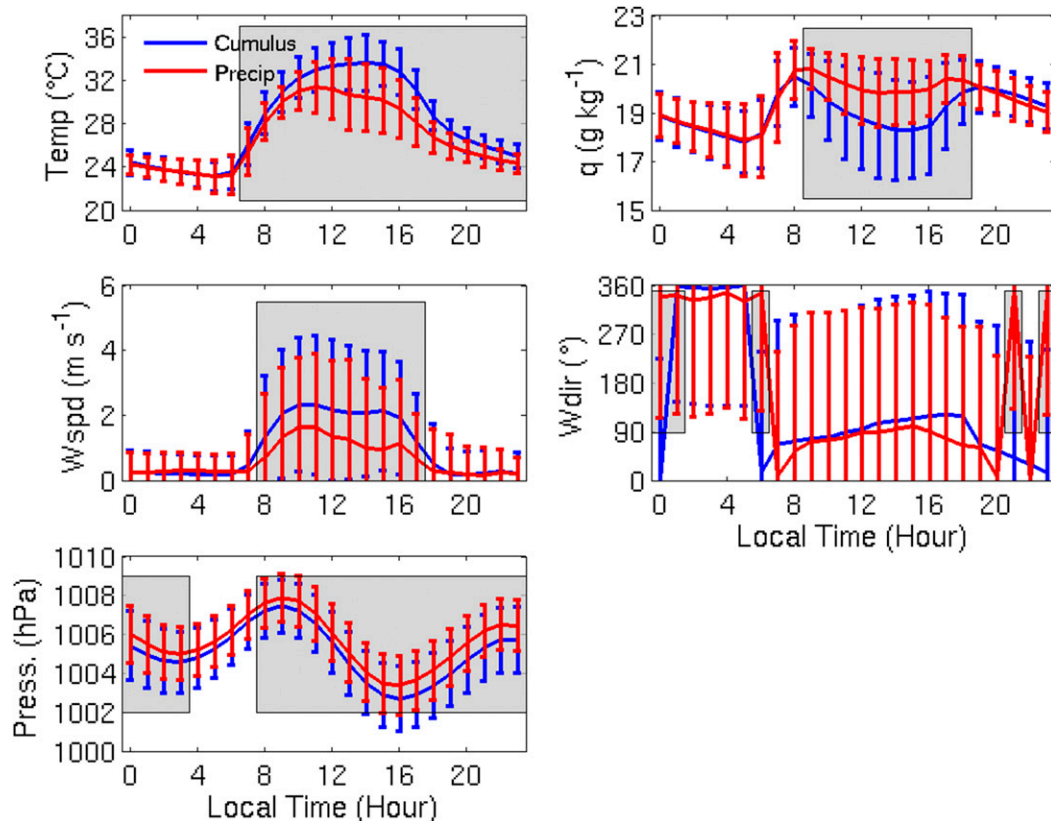


FIG. 9. Diurnal cycle of surface (top left) temperature, (top right) water vapor mixing ratio, (middle left) wind speed, (middle right) wind direction, and (bottom left) surface pressure for cumulus (blue) and daytime precipitation (red) days. The vertical bars indicate one std dev of the parameters. The gray boxes indicate times when the differences between the two diurnal cycles were statistically significant.

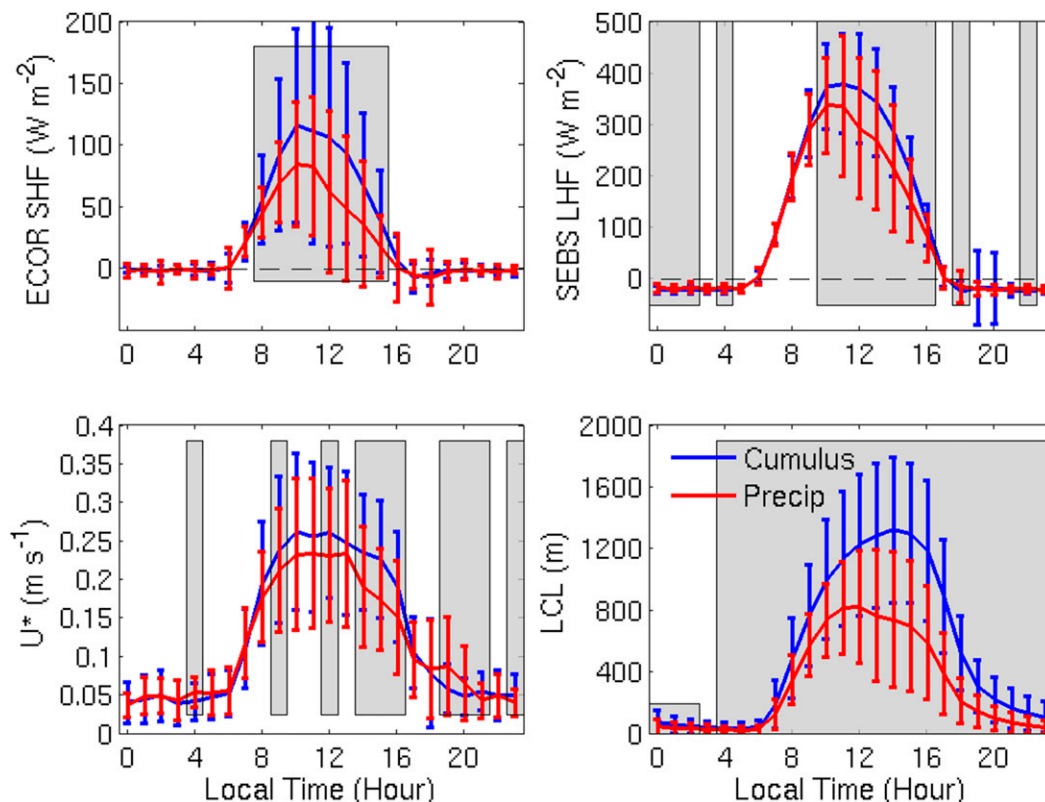


FIG. 10. Diurnal cycle of (top left) SHF, (top right) LHF, (bottom left) friction velocity, and (bottom right) LCL for cumulus (blue) and daytime precipitation (red) days. The vertical bars indicate one std dev of the parameters. The gray boxes indicate times when the difference between the two diurnal cycles were statistically significant.

advection was “spotty” and positive (moist advection) during both cumulus and precipitation days at all hours. While above 700 up to 500 hPa, the moisture advection was negative (dry advection) during cumulus days, with the dry layer extending to ~ 900 hPa during the afternoon hours. The large-scale vertical velocity was similar for the distinction except a bit stronger, with a higher extent (~ 400 hPa) during precipitation days than that during cumulus days (~ 700 hPa). Broadly synthesizing, the plot suggests the advection of moisture above the boundary layer to be the key difference between cumulus and precipitation days, which is in agreement with previous studies (e.g., Zhang and Klein 2010).

To assess the differences in key parameters for precipitating and nonprecipitating days, their averaged values for the entire dry season, for cumulus-only days, and for daytime precipitation days are listed in Table 1. The t value of the statistical significance from a Student’s t distribution assuming a two-tailed Gaussian distribution of the differences in the values of cumulus and precipitation days is also listed in Table 1. As anticipated from our analysis, statistically significant differences are present in the surface air temperature, moisture, and the LCL between cumulus

and daytime precipitation days. The CIN was significantly lower during precipitation days, with insignificant changes in CAPE between cumulus and daytime precipitation days. To further explore the higher IWV observed during precipitation days than during cumulus days, we calculated the integrated water vapor amount between surface and 1 km (WV_{0-1km}), between 1 and 3 km (WV_{1-3km}), and between 3 and 6 km (WV_{3-6km}) as reported by the soundings. The water vapor in all three layers was higher during precipitation days than during cumulus days, suggesting a relatively same amount of increase or decrease in the lower tropospheric water vapor as the total. On average, the horizontal moisture advection was negative during cumulus days and positive during precipitation days with large variations. The commonly used indices to predict occurrence of precipitation were calculated from the radiosondes launched at 0800 LT. The CTP did not exhibit any changes between cumulus and precipitation days, while the HI_{low} did, further reinforcing the role of moisture in determining deep convection. The inversion Bowen ratio was lower during cumulus days than during precipitation days because of the higher lapse rate of moisture during cumulus days than

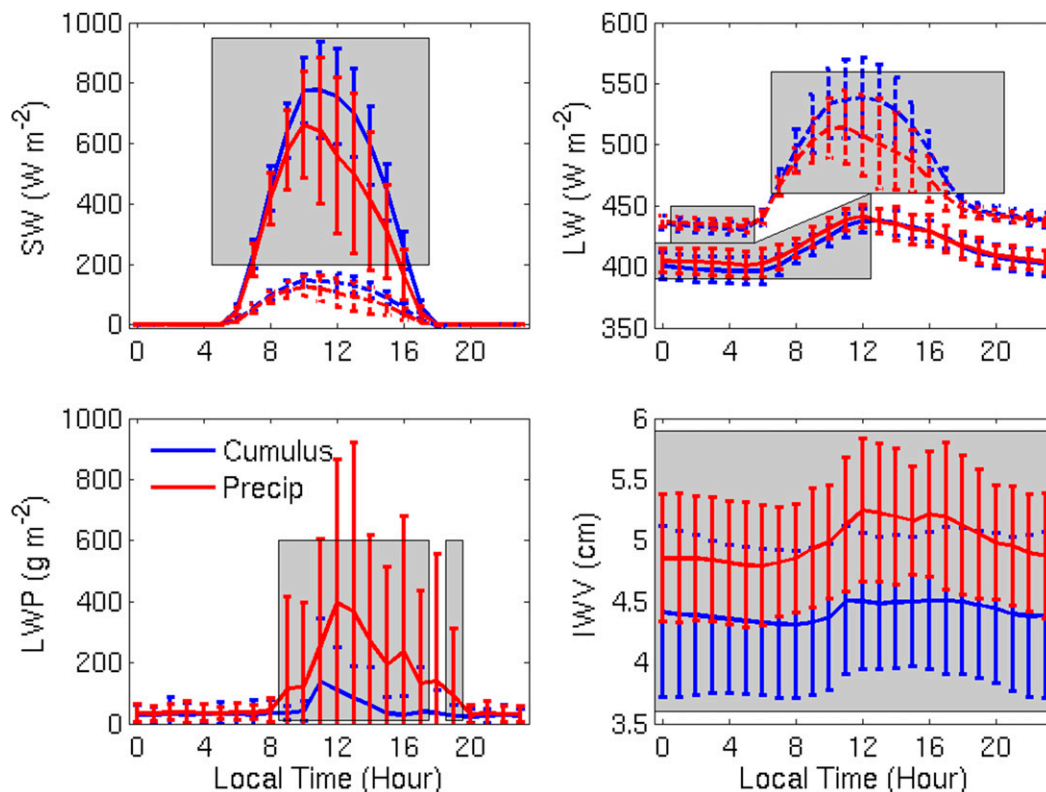


FIG. 11. Diurnal cycle of (top left) shortwave radiation, (top right) longwave radiation, (bottom left) LWP, and (bottom right) IWV for cumulus (blue) and daytime precipitation (red) days. The solid and dashed lines in the top indicate downwelling and upwelling radiation, respectively. The vertical bars indicate one std dev of the parameters. The gray boxes indicate times when the differences between the two diurnal cycles were statistically significant.

during precipitation days. The lapse rate of potential temperature did not exhibit any significant differences for the distinction, while the lapse rate of water vapor mixing ratio was significantly lower during precipitation days compared to cumulus days.

5. Variation of key parameters through the dry season

The comparison of the diurnal cycle of surface and profile properties indicated that IWV, horizontal moisture advection above the boundary layer Q_{ten} , SHF, LCL, and CIN differ substantially between cumulus and precipitation days. In addition to changes in these on precipitation days, their temporal variation through the 2014 and 2015 dry seasons is examined in an attempt to interpret the decrease in precipitation events during the progression of the dry season (Fig. 14). The daily values shown of SHF, LCL, and Q_{ten} in Fig. 14 are averages between 0800 and 1800 LT, and the Q_{ten} is averaged from 700 to 600 hPa (3–4.5 km). The daily averaged column water vapor varied between 3 and 6 cm during the dry seasons, with large variations (>2 cm) around days 15 and

78 in 2014 and days 70 and 100 in 2015. The precipitation events mostly coincided with the local maximum of IWV throughout the two dry seasons, with some exceptions like days 45 and 90 of 2015. The SHF remained fairly low with low variability in 2014, while it increased during the progression of the dry season in 2015. Most of the precipitation events coincided with SHF minimum. Similar to IWV, relatively high ($>30 \text{ W m}^{-2}$) changes in SHF can be seen to occur over a span of few days like days 85–90 and 96–102 in the year 2015. The daytime average LCL varied between ~ 200 and ~ 2000 m during the course of the dry seasons, with greater variations in 2015 than in 2014. The variations in LCL were largely due to changes in the surface water vapor mixing ratio rather than the changes in temperature, and they correspond well with the changes in the IWV. The averaged daytime horizontal advection of water vapor between 600 and 700 hPa was weakly negative (dry advection) with several high positive values. Contrary to our expectations from the diurnal cycle analysis, several precipitation events occurred during dry advection conditions (e.g., day 105 in 2014) and precipitation did not occur on some of the days that had high positive values of moisture

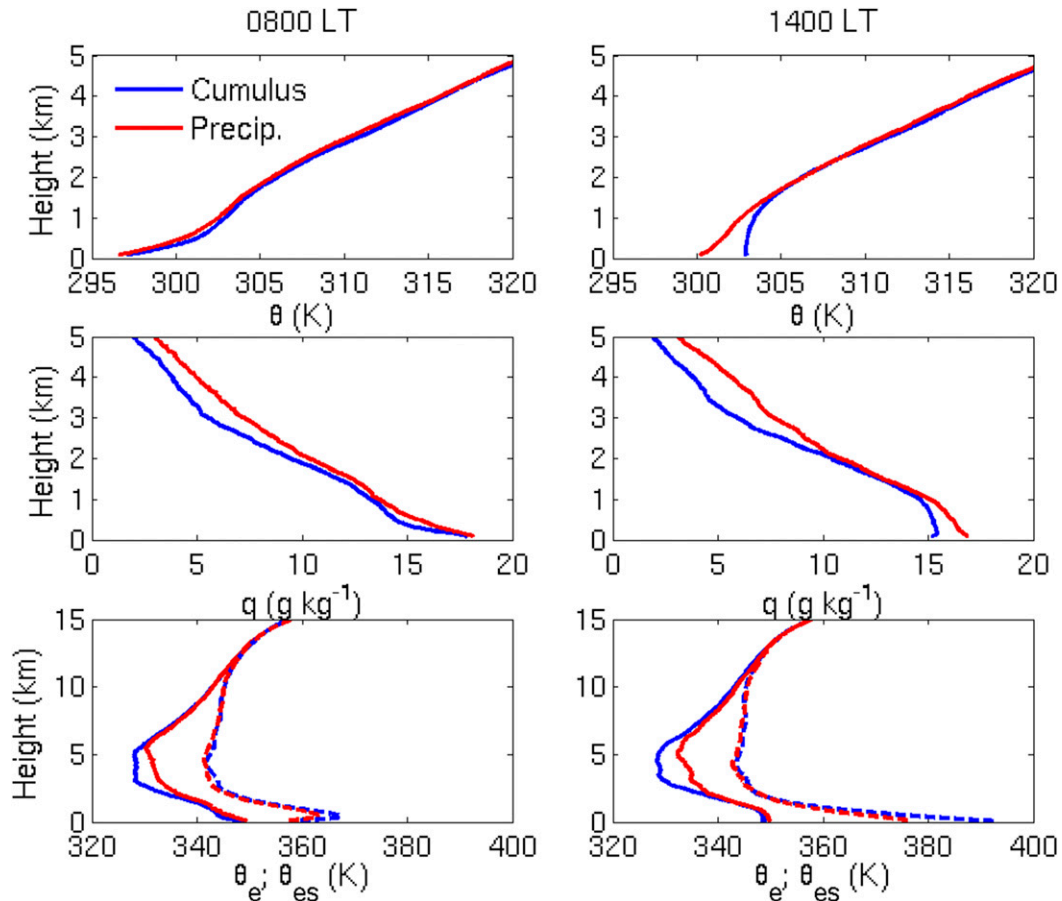


FIG. 12. Averaged profiles of (top) potential temperature, (middle) water vapor mixing ratio, and (bottom) equivalent potential temperature and saturation equivalent potential temperature for cumulus and precipitation days from the soundings launched at (left) 0800 and (right) 1400 LT. The solid lines in the bottom denote the equivalent potential temperature and dashed lines denote the saturation equivalent potential temperature.

advection (e.g., days 36 and 90 in 2015). This suggests that the moisture advection is a secondary parameter determining precipitation. The CIN calculated from the sounding launched at 0800 LT varied from about -50 J kg^{-1} at the beginning of the dry season to in excess of -250 J kg^{-1} toward the end of the dry season. Most of the precipitation events coincided with local minimum values of CIN. Collectively, these observations suggest the column water vapor decreases and the LCL, SHF, and CIN increase during the progression of the dry season. Most of the precipitation events coincided with the local maximum of the IWV and minimum of LCL, SHF, and CIN. The changes in these parameters are not gradual during the dry season, with large fluctuations occurring over a 3–5-day span embedded within the gradual change in them. Most of all, these observations suggest that the changes occurring during the dry season vary greatly from year to year, as highlighted by SHF during the two years studied here.

The rain recurrence interval t_r was calculated for all precipitation events and for the daytime precipitation events. Similar to Fitzjarrald et al. (2008), we have defined t_r as the time interval between the rain events, with a rain event defined as a continuous period when the hourly averaged rain rate was greater than zero. Rain was recorded at the surface on 106 days through 158 rain events (Table 2), denoting 1.49 rain events per rainy day. Although the number of rainy days was almost equal in 2014 and 2015, there were more rain events in 2014 than 2015. The mean t_r for the two dry seasons was 1.42 days, with slightly lower t_r in 2014 (1.36 days) than in 2015 (1.48 days). About 40% of the rain events had t_r greater than 1 day, with 4.5% having t_r greater than 5 days. The rain recurrence time was ~ 1 day in June and July and greater than 2 days during August and September. The decrease in t_r from August to September was observed during both years and is due to multiple precipitation events occurring

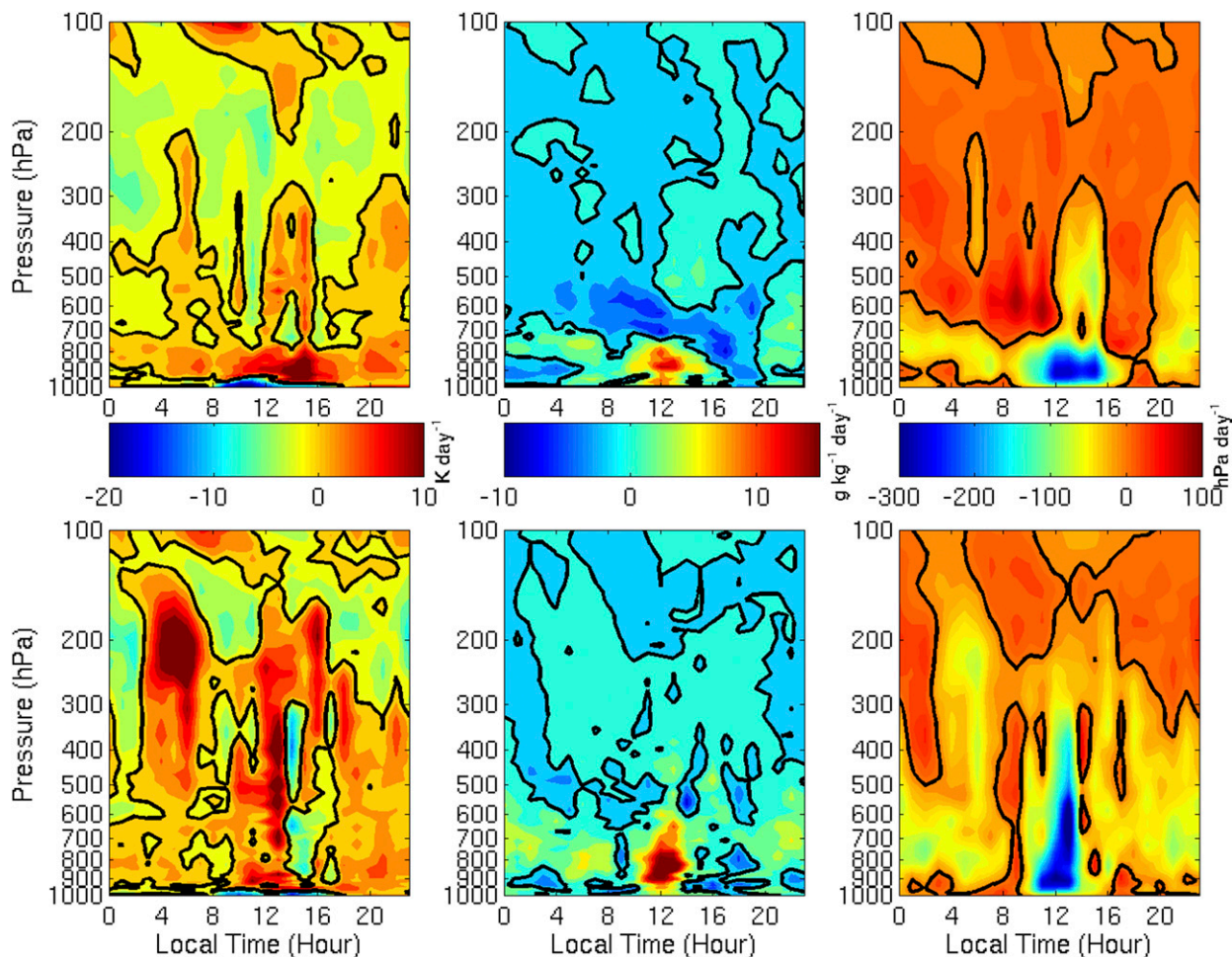


FIG. 13. Average diurnal cycle of the (left) horizontal advection of temperature, (center) horizontal advection of moisture, and (right) large-scale vertical velocity as reported by the ECMWF Re-Analysis for (top) cumulus and (bottom) daytime precipitation days. The black lines denote the zero-value contour.

successively during the first half of September in both years (Fig. 1). About 25 rain events occurred in June and July and about 15 in August and September. Although the number of rain events showed the 2-month cycle, the total accumulated rain for each month showed a gradual decrease from June to September during both years.

As we have focused on daytime precipitation events similar to t_r , we also calculated recurrence time of daytime precipitation events t_{dr} . A total of 82 daytime rain events was observed on the 64 days, denoting 1.28 rain events per daytime precipitation day (Table 3). The average t_{dr} was 2.76 days, with slightly higher t_{dr} in 2015 (2.95) than in 2014 (2.62). The number of daytime precipitation events with t_{dr} greater than 1 day, 5 days, and 10 days was almost equal during the two years. The t_{dr} increased from June to August during both years and then decreased to a mean value of 2.40 days in September. As mentioned earlier, the decrease in t_{dr} in September is due to multiple daytime precipitation

events occurring on consecutive days in the first half of September during both years. The percent of daytime precipitation events of the total rain events together with their share of the accumulated rainfall exhibited an increase each month through the progression of the dry season.

Collectively, this analysis suggests the recurrence time of daytime precipitation events to be higher than that of all precipitation events. The relative change in t_r through the dry season was higher than that of t_{dr} . The number of total rain events and the total accumulated rainfall exhibited a general decrease each month during the progression of the dry season (Table 2), while the percent of daytime precipitation events and their share of accumulated rainfall exhibited a general increase. This suggests the principal decrease in the rainfall during the dry season to be primarily due to reduction in nighttime precipitation that is a result of passing squall lines.

TABLE 1. Mean and std dev of key parameters for the entire dry season (244 days), cumulus-only days (138 days), and daytime precipitation days (64 days). The t value denoting the statistical significance between the values' cumulus and daytime precipitation days from a Student's t distribution is reported in the last column. The average values of LCL and Q_{ten} were calculated for daytime hours only. Values of thermodynamic variables are from the sounding launched at 0800 LT. All other values were calculated from hourly averages.

| Parameter | Dry season | | Cumulus days | | Daytime precipitation days | | $ t $ |
|---|------------|---------|--------------|---------|----------------------------|---------|-------|
| | Mean | Std dev | Mean | Std dev | Mean | Std dev | |
| Surface air temp ($^{\circ}\text{C}$) | 27.51 | 3.89 | 28.09 | 4.22 | 26.82 | 3.48 | 11.02 |
| Surface mixing ratio (g kg^{-1}) | 19.29 | 1.55 | 19.04 | 1.63 | 19.51 | 1.44 | 10.13 |
| LCL (m) | 819.11 | 491.20 | 1010.4 | 493.65 | 608.61 | 373.08 | 21.22 |
| SHF (W m^{-2}) | 23.93 | 51.69 | 28.44 | 58.96 | 18.47 | 41.44 | 6.77 |
| CAPE (J kg^{-1}) | 806.11 | 565.68 | 824.93 | 624.53 | 846.52 | 512.38 | 0.25 |
| CIN (J kg^{-1}) | -88.82 | 53.18 | -98.94 | 58.09 | -76.40 | 37.09 | 3.32 |
| IWV (cm) | 4.71 | 0.67 | 4.41 | 0.61 | 4.98 | 0.53 | 6.77 |
| WV _{0-1km} (cm) | 1.47 | 0.12 | 1.43 | 0.13 | 1.50 | 0.09 | 4.43 |
| WV _{1-3km} (cm) | 2.01 | 0.27 | 1.90 | 0.28 | 2.09 | 0.18 | 5.79 |
| WV _{3-6km} (cm) | 1.08 | 0.42 | 0.90 | 0.38 | 1.20 | 0.32 | 5.83 |
| $Q_{\text{ten}} _{600-700\text{hPa}}$ ($\text{g kg}^{-1}\text{ day}^{-1}$) | -0.27 | 22.59 | -2.60 | 20.14 | 2.48 | 25.48 | 4.65 |
| CTP (J kg^{-1}) | 427.87 | 59.15 | 435.92 | 58.47 | 432.37 | 48.51 | 0.45 |
| HI _{low} ($^{\circ}\text{C}$) | 9.91 | 4.75 | 11.57 | 4.99 | 8.64 | 3.35 | 4.91 |
| $\partial q/\partial z _{1-3\text{km}}$ ($\text{g kg}^{-1}\text{ km}^{-1}$) | -3.58 | 1.05 | -3.86 | 1.12 | -3.21 | 0.84 | 4.58 |
| $\partial\theta/\partial z _{1-3\text{km}}$ (K km^{-1}) | 4.01 | 0.74 | 4.00 | 0.76 | 3.91 | 0.75 | 0.79 |
| B_{inv} | 0.47 | 0.13 | 0.43 | 0.12 | 0.50 | 0.11 | 4.08 |

6. Summary, discussion, and conclusions

The coverage of the Amazon rain forest critically depends on the dry season precipitation. The deployment of the AMF-1 for 2 years in the context of the GOAmazon field campaign provided comprehensive measurements of surface, clouds, radiation, and thermodynamic properties for two complete dry seasons. Precipitation was recorded at the surface on 106 days (43%) during the two (2014 and 2015) dry seasons, with some amount of precipitation recorded at all hours. The precipitation events occurring during the nighttime were associated with southerly advection corresponding to propagating storm systems (nonlocal effects). On the contrary, the daytime precipitation events were primarily observed between 1200 and 1600 LT and were a result of local land-atmosphere interactions. The nighttime low-level cloudiness was higher during precipitation days than during nonprecipitation days. This resulted in lower values of net radiation at the surface that further translated to lower values of surface sensible heat flux. The higher low-level cloudiness was accompanied by higher atmospheric moisture that resulted in lower values of LCL and CIN during precipitation days as compared to nonprecipitation days. The horizontal advection of moisture above the boundary layer as reported by the ECMWF Re-Analysis was weakly positive during precipitation days and weakly negative during nonprecipitation days. The tropical South Atlantic is the primary remote source of moisture for the Amazon basin during the austral winter (Drumond et al. 2014).

Collectively, these results suggest the increased water vapor in the lower troposphere to be the primary factor responsible for triggering the transition from shallow to deep convection. This is achieved by lowering the LCL and the CIN and reducing the impact of dry entrainment on cloudy air parcels. The study provides clear indications of a relationship between large-scale moisture advection and precipitation, suggesting that accurate representation of these large-scale features could provide improved representation of the precipitation over the Amazon basin. As the conclusions about moisture advection above the boundary layer are based on ECMWF Re-Analysis and not on observations, we deem the conclusions to be plausible, albeit not exclusive.

Most of the daytime precipitation events occurred during days that exhibited higher moisture content, moist advection above the boundary layer, and lower values of SHF and CIN before the beginning of the precipitation event. However, a few precipitation events did occur during days that did not fit the above criteria. This suggests a complex interplay between the factors responsible for producing precipitation-generating clouds and possible factors other than those considered here to have an impact on precipitation generation. The general lack of similarity between the evolutions of the variables during the two dry seasons (Fig. 14) strongly warrants long-term monitoring of meteorology for that region and suggests that caution is needed in drawing scientific conclusions from limited amounts of data. Notably, the SHF varied little during the 2014 dry season, while it increased almost gradually during the

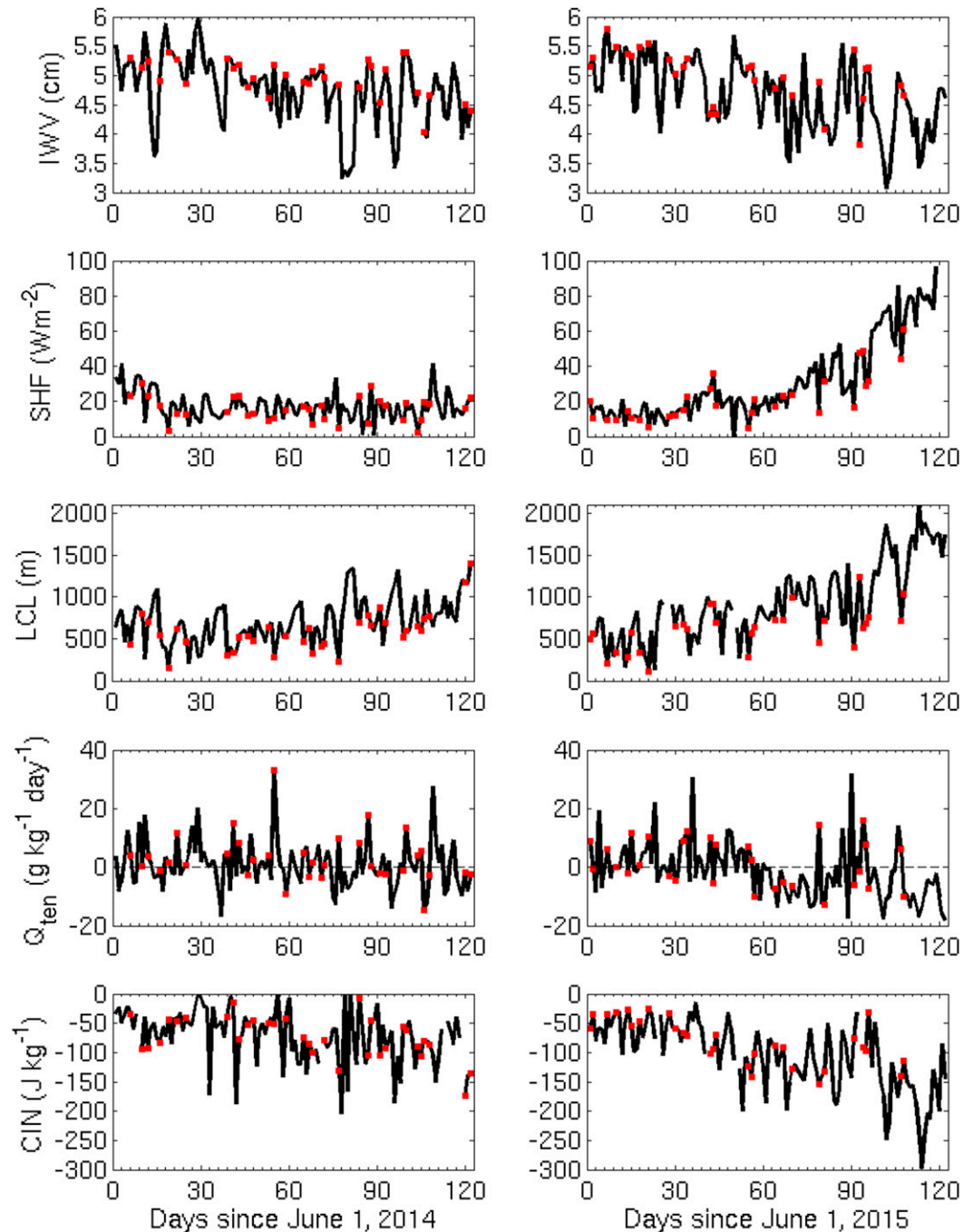


FIG. 14. (from top to bottom) The daily averaged values of IWV, SHF, daytime LCL, daytime moisture tendency between 600 and 700 hPa, and CIN from the 0800 LT sounding during the (left) 2014 and (right) 2015 dry seasons. The red squares denote the days with daytime precipitation.

second half of the 2015 dry season. The analysis of recurrence time of all rain events t_r and daytime rain events t_{dr} showed the t_r to increase through the dry season (except September), with comparatively lower variations in t_{dr} . The analysis also showed the percent contribution of accumulated rainfall from daytime rain

events to the total accumulated rainfall to increase through the progression of the dry season. This, together with the prediction by the IPCC GCM (Cook et al. 2012) of the dry season to get longer, suggests the rainfall (if any) during this increased length to be primarily from the daytime precipitation events, which critically

TABLE 2. Rain recurrence time for all rain events during 2014 and 2015 dry seasons. The percent of t_r values greater than 1, 5, and 10 days are reported in parentheses.

| Parameter | All | 2014 | 2015 |
|--------------------------------|-------------|-------------|-------------|
| Number of rainy days | 106 | 54 | 52 |
| Number of rain events | 158 | 86 | 72 |
| Mean t_r (day) | 1.42 | 1.36 | 1.48 |
| Events with $t_r > 1$ | 63 (40.65%) | 32 (37.64%) | 31 (44.28%) |
| Events with $t_r > 5$ | 7 (4.52%) | 4 (4.70%) | 3 (4.28%) |
| Events with $t_r > 10$ | 2 (1.29%) | 1 (1.17%) | 1 (1.42%) |
| Mean June t_r (day) | 1.04 | 0.99 | 1.10 |
| Mean July t_r (day) | 1.01 | 1.09 | 0.93 |
| Mean August t_r (day) | 2.50 | 2.25 | 2.79 |
| Mean September t_r (day) | 2.03 | 1.73 | 2.82 |
| Events in June | 51 | 26 | 25 |
| Events in July | 54 | 26 | 28 |
| Events in August | 26 | 14 | 12 |
| Events in September | 22 | 16 | 6 |
| Accumulation in June (mm) | 77.79 | 42.08 | 35.71 |
| Accumulation in July (mm) | 59.89 | 30.58 | 29.31 |
| Accumulation in August (mm) | 36.53 | 22.89 | 13.64 |
| Accumulation in September (mm) | 27.02 | 21.79 | 5.23 |

depends on the model's ability to simulate the transition from shallow to deep convection and large-scale moisture advection.

In addition to the daytime precipitation events, the region also receives precipitation from northward-propagating storms during the dry season. The 42 precipitation events (39%) occurred entirely or partly during the nighttime (2100–0900 LT), suggesting a significant amount of rainfall from these systems. As these storms develop and propagate because of large-scale weather patterns, factors other than local land–atmosphere

interactions are also partly responsible for the dry season precipitation. However, the large spread and greater fluctuations over short periods in the column integrated water vapor suggest it to be the primary factor controlling meteorology and precipitation in that region (Satyamurty et al. 2013; Sherwood et al. 2010). Although it is challenging to track atmospheric rivers, especially in a tropical environment, we anticipate such an effort to have a huge impact on our understanding of the meteorology and climate of the Amazon and other tropical regions (Schirotter et al. 2016).

TABLE 3. Rain recurrence time for daytime precipitation events during the 2014 and 2015 dry seasons. The percent of t_{dr} values greater than 1, 5, and 10 days are reported in parentheses. The percent contribution of daytime precipitation events to the total precipitation events and to the total accumulated rainfall are also reported in parentheses.

| Parameter | All | 2014 | 2015 |
|--------------------------------|----------------|----------------|----------------|
| Number of daytime rain days | 64 (60.37%) | 34 (62.96%) | 30 (57.69%) |
| Number of rain events | 82 (51.89%) | 45 (52.32%) | 37 (51.38%) |
| Mean t_{dr} (day) | 2.76 | 2.62 | 2.95 |
| Events with $t_{dr} > 1$ | 52 (65%) | 29 (67.44%) | 22 (61.11%) |
| Events with $t_{dr} > 5$ | 13 (16.25%) | 6 (13.95%) | 7 (19.44%) |
| Events with $t_{dr} > 10$ | 4 (5%) | 2 (4.56%) | 2 (5.56%) |
| Mean June t_{dr} (day) | 2.53 | 2.69 | 2.44 |
| Mean July t_{dr} (day) | 2.76 | 2.81 | 2.69 |
| Mean August t_{dr} (day) | 3.44 | 2.63 | 4.82 |
| Mean September t_{dr} (day) | 2.40 | 2.39 | 2.42 |
| Events in June | 20 (39.21%) | 8 (30.76%) | 12 (48%) |
| Events in July | 22 (40.74%) | 12 (46.15%) | 10 (35.71%) |
| Events in August | 19 (73.07%) | 12 (85.71%) | 7 (58.33%) |
| Events in September | 18 (81.81%) | 12 (75%) | 6 (100%) |
| Accumulation in June (mm) | 27.57 (35.44%) | 15.36 (36.50%) | 12.21 (34.19%) |
| Accumulation in July (mm) | 17.90 (29.88%) | 12.20 (39.89%) | 5.70 (19.44%) |
| Accumulation in August (mm) | 27.16 (74.34%) | 19.57 (85.49%) | 7.59 (55.64%) |
| Accumulation in September (mm) | 24.36 (90.15%) | 19.13 (87.79%) | 5.23 (100%) |

Acknowledgments. We thank Dr. Anthony D. Del Genio and Dr. Stephen W. Nesbitt for helpful discussions that led to significant improvement in the manuscript. This work was primarily supported by the U.S. Department of Energy's (DOE) Atmospheric System Research (ASR), an Office of Science, Office of Biological and Environmental Research (BER) program, under Contract DE-AC02-06CH11357 awarded to Argonne National Laboratory and Contract DE-SC00112704 awarded to Brookhaven National Laboratory. This research was also supported by the National Science Foundation (NSF) Grant AGS-1445831 awarded to the University of Chicago. All the data used in this study were obtained from the Atmospheric Radiation Measurement (ARM) program sponsored by the U.S. Department of Energy, Office of Science, Office of Biological and Environmental Research, Climate and Environmental Sciences Division (CESD). We gratefully acknowledge the computing resources provided on Blues, a high-performance computing cluster operated by the Laboratory Computing Resource Center (LCRC) at the Argonne National Laboratory.

REFERENCES

- Anber, U., P. Gentine, S. Wang, and A. H. Sobel, 2015: Fog and rain in the Amazon. *Proc. Natl. Acad. Sci. USA*, **112**, 11 473–11 477, doi:[10.1073/pnas.1505077112](https://doi.org/10.1073/pnas.1505077112).
- Aragao, L., Y. Malhi, N. Barbier, A. Lima, Y. Shimabukuro, L. Anderson, and S. Saatchi, 2008: Interactions between rainfall, deforestation and fires during recent years in the Brazilian Amazonia. *Philos. Trans. Roy. Soc. London*, **B363**, 1779–1785, doi:[10.1098/rstb.2007.0026](https://doi.org/10.1098/rstb.2007.0026).
- Betts, A. K., J. D. Fuentes, M. Garstang, and J. H. Ball, 2002: Surface diurnal cycle and boundary layer structure over Rondônia during the rainy season. *J. Geophys. Res.*, **107**, 8065, doi:[10.1029/2001JD000356](https://doi.org/10.1029/2001JD000356).
- Bolton, D., 1980: The computation of equivalent potential temperature. *Mon. Wea. Rev.*, **108**, 1046–1053, doi:[10.1175/1520-0493\(1980\)108<1046:TCOEPT>2.0.CO;2](https://doi.org/10.1175/1520-0493(1980)108<1046:TCOEPT>2.0.CO;2).
- Burba, G., 2013: *Eddy Covariance Method for Scientific, Industrial, Agricultural, and Regulatory Applications: A Field Book on Measuring Ecosystem Gas Exchange and Areal Emission Rates*. LI-COR Biosciences, 331 pp.
- Cook, B., N. Zeng, and J.-H. Yoon, 2012: Will Amazonia dry out? Magnitude and causes of change from IPCC climate model projections. *Earth Interact.*, **16**, doi:[10.1175/2011EI398.1](https://doi.org/10.1175/2011EI398.1).
- de Gonçalves, L. G. G., and Coauthors, 2013: Overview of the Large-Scale Biosphere–Atmosphere Experiment in Amazonia Data Model Intercomparison Project (LBA-DMIP). *Agric. Meteorol.*, **182–183**, 111–127, doi:[10.1016/j.agrformet.2013.04.030](https://doi.org/10.1016/j.agrformet.2013.04.030).
- de Oliveira, A. P., and D. R. Fitzjarrald, 1993: The Amazon River breeze and the local boundary layer: I. Observations. *Bound.-Layer Meteorol.*, **63**, 141–162, doi:[10.1007/BF00705380](https://doi.org/10.1007/BF00705380).
- , and —, 1994: The Amazon River breeze and the local boundary layer: II. Linear analysis and modelling. *Bound.-Layer Meteorol.*, **67**, 75–96, doi:[10.1007/BF00705508](https://doi.org/10.1007/BF00705508).
- dos Santos, M. J., M. A. F. Silva Dias, and E. D. Freitas, 2014: Influence of local circulations on wind, moisture, and precipitation close to Manaus City, Amazon region, Brazil. *J. Geophys. Res. Atmos.*, **119**, 13 233–13 249, doi:[10.1002/2014JD021969](https://doi.org/10.1002/2014JD021969).
- Drumond, A., J. Marengo, T. Ambrizzi, R. Nieto, L. Moreira, and L. Gimeno, 2014: The role of the Amazon basin moisture in the atmospheric branch of the hydrological cycle: A Lagrangian analysis. *Hydrol. Earth Syst. Sci.*, **18**, 2577–2598, doi:[10.5194/hess-18-2577-2014](https://doi.org/10.5194/hess-18-2577-2014).
- Fernandes, K., A. Giannini, L. Verchot, W. Baethgen, and M. Pinedo-Vasquez, 2015: Decadal covariability of Atlantic SSTs and western Amazon dry-season hydroclimate in observations and CMIP5 simulations. *Geophys. Res. Lett.*, **42**, 6793–6801, doi:[10.1002/2015GL063911](https://doi.org/10.1002/2015GL063911).
- Findell, K. L., and E. A. B. Eltahir, 2003: Atmospheric controls on soil moisture–boundary layer interactions. Part I: Framework development. *J. Hydrometeorol.*, **4**, 552–569, doi:[10.1175/1525-7541\(2003\)004<0552:ACOSML>2.0.CO;2](https://doi.org/10.1175/1525-7541(2003)004<0552:ACOSML>2.0.CO;2).
- Fitzjarrald, D. R., and K. E. Moore, 1990: Mechanisms of nocturnal exchange between the rain forest and the atmosphere. *J. Geophys. Res.*, **95**, 16 839–16 850, doi:[10.1029/JD095iD10p16839](https://doi.org/10.1029/JD095iD10p16839).
- , R. K. Sakai, O. L. L. Moraes, R. C. de Oliveira, O. C. Acevedo, M. J. Czikowsky, and T. Beldini, 2008: Spatial and temporal rainfall variability near the Amazon–Tapajós confluence. *J. Geophys. Res.*, **113**, G00B11, doi:[10.1029/2007JG000596](https://doi.org/10.1029/2007JG000596).
- Gentine, P., A. A. M. Holtslag, F. D'Andrea, and M. Ek, 2013: Surface and atmospheric controls on the onset of moist convection over land. *J. Hydrometeorol.*, **14**, 1443–1462, doi:[10.1175/JHM-D-12-0137.1](https://doi.org/10.1175/JHM-D-12-0137.1).
- Gloor, M., and Coauthors, 2012: The carbon balance of South America: A review of the status, decadal trends and main determinants. *Biogeosciences*, **9**, 5407–5430, doi:[10.5194/bg-9-5407-2012](https://doi.org/10.5194/bg-9-5407-2012).
- Grimm, A. M., 2003: The El Niño impact on the summer monsoon in Brazil: Regional processes versus remote influences. *J. Climate*, **16**, 263–280, doi:[10.1175/1520-0442\(2003\)016<0263:TENIOT>2.0.CO;2](https://doi.org/10.1175/1520-0442(2003)016<0263:TENIOT>2.0.CO;2).
- , 2004: How do La Niña events disturb the summer monsoon system in Brazil? *Climate Dyn.*, **22**, 123–138, doi:[10.1007/s00382-003-0368-7](https://doi.org/10.1007/s00382-003-0368-7).
- Harper, A., I. T. Baker, A. S. Denning, D. A. Randall, D. Dazlich, and M. Branson, 2014: Impact of evapotranspiration on dry season climate in the Amazon forest. *J. Climate*, **27**, 574–591, doi:[10.1175/JCLI-D-13-00074.1](https://doi.org/10.1175/JCLI-D-13-00074.1).
- Harriss, R. C., and Coauthors, 1988: The Amazon Boundary Layer Experiment (ABLE 2A): Dry season 1985. *J. Geophys. Res.*, **93**, 1351–1360, doi:[10.1029/JD093iD02p01351](https://doi.org/10.1029/JD093iD02p01351).
- Joetjzer, E., H. Douville, C. Delire, and P. Ciais, 2013: Present-day and future Amazonian precipitation in global climate models: CMIP5 versus CMIP3. *Climate Dyn.*, **41**, 2921–2936, doi:[10.1007/s00382-012-1644-1](https://doi.org/10.1007/s00382-012-1644-1).
- Juarez, R. I. N., M. G. Hodnett, R. Fu, M. Goulden, and C. von Randow, 2007: Control of dry season evapotranspiration over Amazonian forest as inferred from observations at a southern Amazon forest site. *J. Climate*, **20**, 2827–2839, doi:[10.1175/JCLI4184.1](https://doi.org/10.1175/JCLI4184.1).
- Kaufman, Y. J., and Coauthors, 1998: Smoke, Clouds, and Radiation—Brazil (SCAR-B) experiment. *J. Geophys. Res.*, **103**, 31 783–31 808, doi:[10.1029/98JD02281](https://doi.org/10.1029/98JD02281).
- Kollias, P., M. A. Miller, K. L. Johnson, M. P. Jensen, and D. T. Troyan, 2009: Cloud, thermodynamic, and precipitation observations in West Africa during 2006. *J. Geophys. Res.*, **114**, D00E08, doi:[10.1029/2008JD010641](https://doi.org/10.1029/2008JD010641).

- Lewis, S. L., P. M. Brando, O. L. Phillips, G. M. Van der Heijden, and D. Nepstad, 2011: The 2010 Amazon drought. *Science*, **331**, 554, doi:[10.1126/science.1200807](https://doi.org/10.1126/science.1200807).
- Li, W., and R. Fu, 2004: Transition of the large-scale atmospheric and land surface conditions from the dry to the wet season over Amazonia as diagnosed by the ECMWF Re-Analysis. *J. Climate*, **17**, 2637–2651, doi:[10.1175/1520-0442\(2004\)017<2637:TOTLAA>2.0.CO;2](https://doi.org/10.1175/1520-0442(2004)017<2637:TOTLAA>2.0.CO;2).
- Liebmann, B., and C. R. Mechoso, 2011: The South American Monsoon System. *The Global Monsoon System: Research and Forecast*, 2nd ed., C.-P. Chang et al., Eds., World Scientific Series on Asia-Pacific Weather and Climate, Vol. 5, World Scientific, 608 pp.
- Luo, Z., and W. B. Rossow, 2004: Characterizing tropical cirrus life cycle, evolution, and interaction with upper-tropospheric water vapor using Lagrangian trajectory analysis of satellite observations. *J. Climate*, **17**, 4541–4563, doi:[10.1175/3222.1](https://doi.org/10.1175/3222.1).
- Malhi, Y., and Coauthors, 2009: Exploring the likelihood and mechanism of a climate-change-induced dieback of the Amazon rainforest. *Proc. Natl. Acad. Sci. USA*, **106**, 20 610–20 615, doi:[10.1073/pnas.0804619106](https://doi.org/10.1073/pnas.0804619106).
- Martin, C. L., D. Fitzjarrald, M. Garstang, A. P. Oliveira, S. Greco, and E. Browell, 1988: Structure and growth of the mixing layer over the Amazonian rain forest. *J. Geophys. Res.*, **93**, 1361–1375, doi:[10.1029/JD093iD02p01361](https://doi.org/10.1029/JD093iD02p01361).
- Mather, J. H., and J. W. Voyles, 2013: The ARM climate research facility: A review of structure and capabilities. *Bull. Amer. Meteor. Soc.*, **94**, 377–392, doi:[10.1175/BAMS-D-11-00218.1](https://doi.org/10.1175/BAMS-D-11-00218.1).
- Mehran, A., A. AghaKouchak, and T. J. Phillips, 2014: Evaluation of CMIP5 continental precipitation simulations relative to satellite-based gauge-adjusted observations. *J. Geophys. Res. Atmos.*, **119**, 1695–1707, doi:[10.1002/2013JD021152](https://doi.org/10.1002/2013JD021152).
- Misra, V., 2008: Coupled air, sea, and land interactions of the South American monsoon. *J. Climate*, **21**, 6389–6403, doi:[10.1175/2008JCLI2497.1](https://doi.org/10.1175/2008JCLI2497.1).
- Pereira Filho, A. J., M. A. F. Silva Dias, R. I. Albrecht, L. G. P. Pereira, A. W. Gandu, O. Massambani, A. Tokay, and S. Rutledge, 2002: Multisensor analysis of a squall line in the Amazon region. *J. Geophys. Res.*, **107**, 8084, doi:[10.1029/2000JD000305](https://doi.org/10.1029/2000JD000305).
- Phillips, O., and Coauthors, 2009: Drought sensitivity of the Amazon rainforest. *Science*, **323**, 1344–1347, doi:[10.1126/science.1164033](https://doi.org/10.1126/science.1164033).
- Raia, A., and I. F. A. Cavalcanti, 2008: The life cycle of the South American monsoon system. *J. Climate*, **21**, 6227–6246, doi:[10.1175/2008JCLI2249.1](https://doi.org/10.1175/2008JCLI2249.1).
- Rickenbach, T. M., 2004: Nocturnal cloud systems and the diurnal variation of clouds and rainfall in southwestern Amazonia. *Mon. Wea. Rev.*, **132**, 1201–1219, doi:[10.1175/1520-0493\(2004\)132<1201:NCSATD>2.0.CO;2](https://doi.org/10.1175/1520-0493(2004)132<1201:NCSATD>2.0.CO;2).
- Saatchi, S., and Coauthors, 2011: Benchmark map of forest carbon stocks in tropical regions across three continents. *Proc. Natl. Acad. Sci. USA*, **108**, 9899–9904, doi:[10.1073/pnas.1019576108](https://doi.org/10.1073/pnas.1019576108).
- , S. Asefi-Najafabady, U. Malhi, L. E. O. C. Aragão, L. O. Anderson, R. B. Myneni, and R. Nemani, 2013: Persistent effects of severe drought on Amazonian forest canopy. *Proc. Natl. Acad. Sci. USA*, **110**, 565–570, doi:[10.1073/pnas.1204651110](https://doi.org/10.1073/pnas.1204651110).
- Satyamurty, P., C. P. W. da Costa, and A. O. Manzi, 2013: Moisture source for the Amazon basin: A study of contrasting years. *Theor. Appl. Climatol.*, **111**, 195–209, doi:[10.1007/s00704-012-0637-7](https://doi.org/10.1007/s00704-012-0637-7).
- Schiro, K. A., J. D. Neelin, D. K. Adams, and B. R. Lintner, 2016: Deep convection and column water vapor over tropical land versus tropical ocean: A comparison between the Amazon and the tropical western Pacific. *J. Atmos. Sci.*, **73**, 4043–4063, doi:[10.1175/JAS-D-16-0119.1](https://doi.org/10.1175/JAS-D-16-0119.1).
- Sherwood, S. C., R. Roca, T. M. Weckwerth, and N. G. Andronova, 2010: Tropospheric water vapor, convection, and climate. *Rev. Geophys.*, **48**, RG2001, doi:[10.1029/2009RG000301](https://doi.org/10.1029/2009RG000301).
- Silva Dias, M. A. F., and Coauthors, 2002a: A case study of convective organization into precipitating lines in the southwest Amazon during the WETAMC and TRMM-LBA. *J. Geophys. Res.*, **107**, 8078, doi:[10.1029/2001JD000375](https://doi.org/10.1029/2001JD000375).
- Spracklen, D. V., S. R. Arnold, and C. M. Taylor, 2012: Observations of increased tropical rainfall preceded by air passage over forests. *Nature*, **489**, 282–285, doi:[10.1038/nature11390](https://doi.org/10.1038/nature11390).
- Stull, R. B., 1988: *An Introduction to Boundary Layer Meteorology*. Kluwer Academic, 666 pp.
- Tanaka, L. M. S., P. Satyamurty, and L. A. T. Machado, 2014: Diurnal variations of precipitation in central Amazon basin. *Int. J. Climatol.*, **34**, 3574–3584, doi:[10.1002/joc.3929](https://doi.org/10.1002/joc.3929).
- Toomey, M., D. A. Roberts, C. Still, M. L. Goulden, and J. P. McFadden, 2011: Remotely sensed heat anomalies linked with Amazonian forest biomass declines. *Geophys. Res. Lett.*, **38**, L19704, doi:[10.1029/2011GL049041](https://doi.org/10.1029/2011GL049041).
- Werth, D., and R. Avissar, 2002: The local and global effects of Amazon deforestation. *J. Geophys. Res.*, **107**, 8087, doi:[10.1029/2001JD000717](https://doi.org/10.1029/2001JD000717).
- Wohlfahrt, G., and P. Widmoser, 2013: Can an energy balance model provide additional constraints on how to close the energy imbalance? *Agric. For. Meteorol.*, **169**, 85–91, doi:[10.1016/j.agrformet.2012.10.006](https://doi.org/10.1016/j.agrformet.2012.10.006).
- Yoon, J.-H., 2016: Multi-model analysis of the Atlantic influence on southern Amazon rainfall. *Atmos. Sci. Lett.*, **17**, 122–127, doi:[10.1002/asl.600](https://doi.org/10.1002/asl.600).
- Zhang, Y., and S. A. Klein, 2010: Mechanisms affecting the transition from shallow to deep convection over land: Inferences from observations of the diurnal cycle collected at the ARM Southern Great Plains site. *J. Atmos. Sci.*, **67**, 2943–2959, doi:[10.1175/2010JAS3366.1](https://doi.org/10.1175/2010JAS3366.1).
- , and —, 2013: Factors controlling the vertical extent of fair-weather shallow cumulus clouds over land: Investigation of diurnal-cycle observations collected at the ARM Southern Great Plains site. *J. Atmos. Sci.*, **70**, 1297–1315, doi:[10.1175/JAS-D-12-0131.1](https://doi.org/10.1175/JAS-D-12-0131.1).